



# An electrochemical modeling of lithium-ion battery nail penetration



Kuan-Cheng Chiu<sup>a</sup>, Chi-Hao Lin<sup>b</sup>, Sheng-Fa Yeh<sup>b</sup>, Yu-Han Lin<sup>b</sup>, Kuo-Ching Chen<sup>a,\*</sup>

<sup>a</sup> Institute of Applied Mechanics, National Taiwan University, No. 1, Sec. 4, Roosevelt Road, Taipei 10617, Taiwan

<sup>b</sup> Material and Chemical Research Laboratories, Industrial Technology Research Institute, 195, Sec. 4, Chung Hsing Rd., Chutung, Hsinchu 31040, Taiwan

## HIGHLIGHTS

- The experiment and simulation of LIB nail penetration test are performed.
- We model the behavior of short-circuit LIBs using porous electrode theory.
- Accurately describing the short-circuit voltage is essential.
- Nail penetration induced thermal runaway is described by abuse equations.
- The short-circuit heating determines the moment of thermal runaway.

## ARTICLE INFO

### Article history:

Received 7 September 2013

Received in revised form

10 November 2013

Accepted 22 November 2013

Available online 1 December 2013

### Keywords:

Lithium-ion battery

Nail penetration

Short-circuit modeling

Thermal runaway

## ABSTRACT

Nail penetration into a battery pack, resulting in a state of short-circuit and thus burning, is likely to occur in electric car collisions. To demonstrate the behavior of a specific battery when subject to such incidents, a standard nail penetration test is usually performed; however, conducting such an experiment is money consuming. The purpose of this study is to propose a numerical electrochemical model that can simulate the test accurately. This simulation makes two accurate predictions. First, we are able to model short-circuited lithium-ion batteries (LIBs) via electrochemical governing equations so that the mass and charge transfer effect could be considered. Second, the temperature variation of the cell during and after nail penetration is accurately predicted with the help of simulating the temperature distribution of thermal runaway cells by thermal abuse equations. According to this nail penetration model, both the onset of battery thermal runaway and the cell temperature profile of the test are obtained, both of which are well fitted with our experimental results.

© 2013 Elsevier B.V. All rights reserved.

## 1. Introduction

Lithium-ion batteries (LIBs) are widely used in portable electronic devices. With characteristics of high power density and little memorizing effect, LIBs are now also being utilized as the power source for electric-powered transportation tools, such as EVs (electric vehicles) and HEVs (hybrid electric vehicles) [1,2]. Since passenger safety is closely related to the vehicle's design, a thorough understanding of the EV's and HEV's LIB behavior under extreme environment is essential, especially in abuse conditions which can potentially cause inflammation or explosion of the battery pack. As a result, various tests can be conducted to give an insight of the battery's property under different abuse conditions.

\* Corresponding author. Tel.: +886 2 3366 5676; fax: +886 2 2363 9290.

E-mail addresses: [kcc@spring.iam.ntu.edu.tw](mailto:kcc@spring.iam.ntu.edu.tw), [kuochingchen@ntu.edu.tw](mailto:kuochingchen@ntu.edu.tw) (K.-C. Chen).

In this paper, we focus on one test—the nail penetration test [3–6]—for battery safety. By driving a steel nail directly into the LIB, the negative and positive electrodes are partially connected inside the jelly-roll by the electric conducting nail. At the point of penetration, electrons can flow freely between the two electrodes through the nail, resulting in a local internal short-circuit that occurs at the nail and jelly-roll interface. Joule and entropic heat are thus generated due to the large electric current density and the redox reaction of lithium, respectively [7]. This excessive heat will propagate throughout the cell from the point of penetration, raising the temperature of the jelly-roll within. If no current shut-down or temperature suppressing device is effective, the cell temperature could upsurge high enough to trigger the thermal decomposing reactions of the jelly-roll materials. Once the reactions are activated, it is generally inescapable for battery thermal runaway to occur [8].

By conducting the battery nail penetration test, valuable information about the behavior of batteries under internal short-circuit

could be provided. However, such experiments may be money consuming, and with the potential of battery explosion, nail penetration must take place inside a fire-proof infrastructure, causing it a dangerous test to conduct.

Besides experiments, numerical methods provide a sensible alternative means to save money. Modeling the nail penetration includes the simulation of (i) LIB short-circuit and (ii) material thermal decomposition. When encountering LIB short-circuit, the heat generation rate can be simulated by considering only the ohmic heating of the cell due to a large current density discharge [9,10]. However, a more sophisticated method is to consider the entropic heating as well, and the temperature of the battery can be simulated if the thermal properties of the cell are known [11–14]. On the other hand, a crush experiment could be performed to understand the effect of internal short-circuit due to physical abuse [15]. The experiment reveals the situation when LIBs are dropped or bent by an outer force. Another condition of LIB short-circuit is the contamination of metal particle during manufacturing, and studies have shown that there is a significant difference between the cell behaviors of nail penetration induced and contamination induced short-circuit [16].

In this work, Section 2 presents the setup and the experimental results of the nail penetration test. Section 3 describes the improvement of battery short-circuit simulation by simulating the battery short-circuit process via electrochemical governing equations and by considering both the Joule and entropic heat generation rates. In so doing, the initial heating of the battery after penetration, which accounts for the triggering of thermal runaway, can be modeled by a more rigorous treatment. Moreover, the influence of cell parameters on battery heating, such as the state of charge (SOC), could also be qualitatively and quantitatively analyzed. In addition to battery short-circuit, we adopted thermal abuse equations [17,18], described in Section 4, to accurately model the exothermic material decomposition of LIB materials when exposed to high temperature. We believe an exact characterization of the reaction's heat generation rate is essential for evaluating the effectiveness of a specific battery pack nail penetration safety design. In Section 5, we combine the LIB short-circuit simulation approach of Section 3 and the thermal abuse equations of Section 4 to construct the LIB nail penetration model. Section 6 is a conclusion.

## 2. Nail penetration test of LIBs

The experiment setup of the nail penetration test is shown in Fig. 1. The type of LIB we used in the test is an ITRI (Industrial Technology Research Institute of Taiwan) 5.25 Ah lithium manganese oxide (LMO) soft package prismatic cell, initially charged to

100% SOC before penetration. The cell was fresh, and no additional safety designs to prevent the battery from short-circuit or thermal runaway were embedded within. A total of five thermal couples, mounted at locations as indicated in Fig. 1(a), were used to record the battery surface temperature. The picture of the actual battery and thermal couple layout is shown in Fig. 1(b). A 3 mm diameter stainless steel nail was used as the penetrating nail. The point of penetration was located at the center of the battery, with the penetrating direction being perpendicular to the battery surface. The nail was programmed to penetrate through the cell with the speed of  $10 \text{ mm s}^{-1}$ , and remains in the cell throughout the experiment. The whole nail penetration test was conducted inside an explosion-proof chamber, with ventilation turned on after penetration occurred. Initial temperature of the battery and the ambient was kept at  $25.7^\circ\text{C}$ . Due to a possibility of battery dilation, two fixed Bakelites were in direct contact with the top and bottom surfaces of the cell to prevent the thermal couples from detaching during the test.

The temperature evolution recorded by each thermal couple is shown in Fig. 2, where there is a sudden jump of cell temperature to over  $300^\circ\text{C}$  at approximately 50 s after nail penetration. This abrupt rise of temperature indicates the occurrence of battery thermal runaway. Furthermore, thermal couple E captured the greatest temperature peak value of the five, while the two smallest peaks were recorded by thermal couples C and D. Near the center of the cell, where short-circuit took place, thermal couple E received the maximum heat from short-circuit and minimum cooling from ventilation. In contrast, the peaks were smallest in thermal couples C and D as they were located far away from the point of penetration and near the edge of the battery, where convection had the strongest effect.

## 3. LIB short-circuit simulation

For simulating LIBs operating under normal conditions, the porous electrode theory [19–24], presented in the following paragraph with a concise description, provides a background of the battery's electric and mass transfer process. The theory usually treats the temperature as a constant parameter and simplifies the jelly-roll of the cell to a one-dimensional geometry that is composed of five segments, which correspond to the thickness of the two current collectors and electrodes and the separator. Fig. 3 is an example of the structure, where  $L$  is the cell thickness and the leftmost boundary of the negative electrode current collector is set as the origin of the  $x^*$ -axis, which is the theory's one-dimensional coordinate.

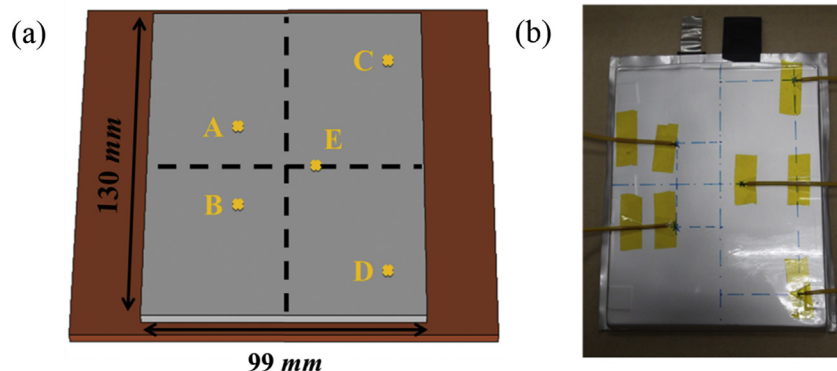


**Fig. 1.** The layout of the ITRI 5.25 Ah soft package prismatic cell nail penetration test with the upper Bakelite removed for a clearer observation. (a) The cell has a  $99 \times 130 \text{ mm}^2$  cross-sectional area and 5 mm thick. The mounting coordinates, with the origin at the center of the cell, for thermal couples A, B, C, D, and E are  $(-2, 2)$ ,  $(-2, -2)$ ,  $(3.5, 5)$ ,  $(3.5, -5)$ , and  $(1, 0)$ , respectively. (b) A photo image of the actual test setup with the five mounted thermal couples.

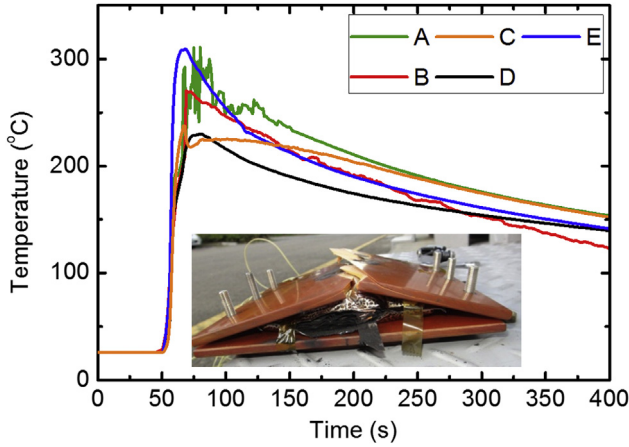


**Fig. 2.** Experimental result of the ITRI 5.25 Ah soft package prismatic cell nail penetration test. The five temperature curves are obtained by the measurement of the corresponding thermal couples shown in Fig. 1(a). The inset is a photograph of the test setup after the penetration. Although the cell generated large internal pressure due to thermal runaway and broke the upper Bakelite, the five thermal couples remained attached to the cell properly.

From the porous electrode theory, Fick's second law of diffusion is applied to evaluate the change of lithium concentration due to solid phase diffusion inside the negative and positive electrodes of the battery [25–27]:

$$\frac{\partial c_{s,i}}{\partial t} = D_{s,i} \left[ \frac{\partial^2 c_{s,i}}{\partial r^2} + \frac{2}{r} \frac{\partial c_{s,i}}{\partial r} \right], \quad i = n, p, \quad (1)$$

where  $r$  is the radial coordinate of the electrode's particle. Ohm's law describes the connection between solid phase current density and the solid phase electric potential gradient:

$$I_{s,i} = -\sigma_{s,i}^{\text{eff}} \nabla^* \phi_{s,i}, \quad i = n, p, \quad (2)$$

where the effective solid phase electric conductivity is calculated by  $\sigma_{s,i}^{\text{eff}} = \sigma_{s,i}(1 - \varepsilon_{s,i} - \varepsilon_{f,i})$ , and  $\nabla^* = \partial/\partial x^*$  is the gradient operator with respect to the model's one-dimensional coordinate. An alternative form of Faraday's law relates the solid phase current density gradient and the pore wall lithium-ion flux:

$$\nabla^* I_{s,i} = -F a_i j_{\text{Li},i}, \quad i = n, p, \quad (3)$$

where  $F$  is the Faraday constant and  $a_i$  is the specific interfacial area, determined by  $a_i = 3(1 - \varepsilon_{s,i} - \varepsilon_{f,i})/R_{s,i}$  with the radius of electrode particle  $R_{s,i}$ . The magnitude and direction of the flux is calculated by

the Butler–Volmer equation, which describes the difference between reduction and oxidation reaction rates of lithium at the electrode–electrolyte interface:

$$j_{\text{Li},i} = k_{s,i}(c_i)^{0.5} (c_{s,i}^{\text{M}} - c_{s,i}^{\text{surf}})^{0.5} (c_{s,i}^{\text{surf}})^{0.5} \times \left\{ \exp \left[ \frac{F \eta_{s,i}}{2RT} \right] - \exp \left[ \frac{-F \eta_{s,i}}{2RT} \right] \right\}, \quad i = n, p, \quad (4)$$

where  $\eta_{s,i} = \phi_{s,i} - \phi_{l,i} - U_i^c - F j_{\text{Li},i} R_{f,i}$  is the surface over-potential. The mass transfer process inside electrolyte phase in the separator region, negative electrode, and positive electrode includes the diffusion of lithium-salt, cations, and anions:

$$\varepsilon_{l,i} \frac{\partial c_i}{\partial t} = \nabla^* \cdot (D_{l,i}^{\text{eff}} \nabla^* c_i) - \frac{I_{l,i} \cdot \nabla^* t^+}{F} + a_i j_{\text{Li},i} (1 - t^+), \quad i = e, n, p, \quad (5)$$

where lithium-ion diffusivity of the electrolyte phase is corrected by the Bruggeman exponential  $\gamma$  as  $D_{l,i}^{\text{eff}} = D_{l,i} \gamma$ . Potential distribution across the electrolyte phase with respect to its current density is evaluated by the modified Ohm's law:

$$I_{l,i} = -\kappa_{l,i} \nabla^* \phi_{l,i} + \frac{2\kappa_{l,i}^{\text{eff}} RT}{F} (1 - t^+) \nabla^* \ln c_i, \quad i = e, n, p. \quad (6)$$

An alternative form of Faraday's law, similar to Equation (3), is used to link the electrolyte phase current density gradient and the pore wall lithium-ion flux:

$$\nabla^* I_{l,i} = F a_i j_{\text{Li},i}, \quad i = n, p. \quad (7)$$

### 3.1. Short-circuit simulation setup

Short-circuit of battery indicates that the positive electrode's electric potential value ( $\phi_{s,p}$ ) is very close to the negative electrode's ( $\phi_{s,n}$ ). To simulate short-circuit, we modified the porous electrode theory by artificially giving a potential value at the positive end of the battery ( $x^* = L$ ), which serves as a boundary condition in the numerical model, i.e.,  $\phi_{s,p}(x^*, t)|_{x^*=L} = \phi_{s,p}(L, t)$  with  $\phi_{s,p}(L, t)$  being given. Initially, for the simplest case possible, we assumed that  $\phi_{s,p}(L, t) = 0.5$  V (relative to ground) and it would be kept constant throughout the whole short-circuit process. However, previous experiment results showed that  $\phi_{s,p}$  decayed with time soon after short-circuit occurred [28,29]. Therefore, we reconsidered  $\phi_{s,p}(L, t)$  as  $\phi_{s,p}(L, t) = 0.5 \exp(-0.07t)$  V, which is a close fit of electric potential to the experimentally measured time decaying profile.

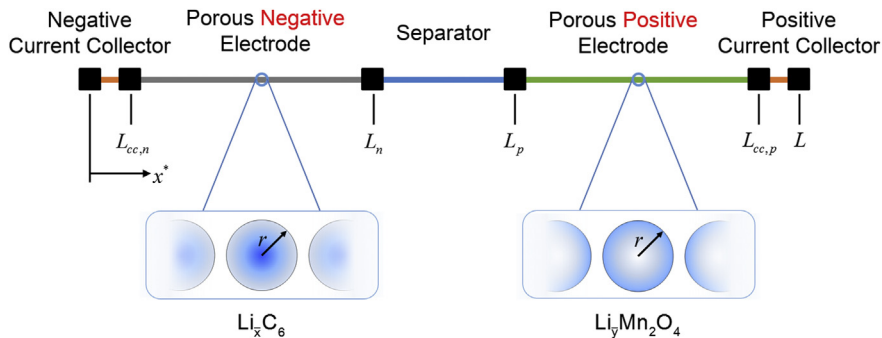


**Fig. 3.** The one-dimensional geometry in the porous electrode theory.

Battery short-circuit causes a severe rise of cell temperature. To simulate the corresponding heating of the battery, we utilized the simplified form of LIB heat generation rate provided by Bernardi et al. [30]:

$$S_{sc} = \sum_i \left[ a_i I_{s,i} (U_i^c - \phi_{s,i}) - a_i I_{s,i} \left( T \frac{\partial U_i^c}{\partial T} \right) \right], \quad i = n, p, \quad (8)$$

which was frequently adopted in LIB thermal analysis [8,31–37]. There are two major heat sources produced by the electrochemical process of LIBs: the irreversible Joule heating and the reversible entropic heating. They are represented by the first and second term of Equation (8), respectively. The entropy of the carbon negative electrode  $\text{Li}_x\text{C}_6$  is provided by Srinivasan et al. [38] in the form of:

$$\frac{dU_n^c}{dT_s} = \frac{344.1347148 \exp(-32.9633287\bar{x} + 8.316711484)}{1 + 749.0756003 \exp(-34.79099646\bar{x} + 8.887143624)} - 0.8520278805\bar{x} + 0.362299229\bar{x}^2 + 0.2698001697, \quad (9)$$

and the entropy of the  $\text{Li}_{1-x}\text{Mn}_2\text{O}_4$  positive electrode is given as:

It should be noted that the unit of the two electrodes' entropy presented in Equations (9) and (10) is  $\text{mV K}^{-1}$ . Since  $S_{sc}$  is dependent on the electric potential (as well as solid phase current density

$$\begin{aligned} \frac{dU_p^c}{dT_s} = & 4.31274309 \exp(0.571536523\bar{y}) + 1.281681122 \sin(-4.9916739\bar{y}) - 0.090453431 \sin(-20.9669665\bar{y} + 12.5788250) \\ & - 0.0313472974 \sin(31.7663338\bar{y} - 22.4295664) - 4.14532933 + 8.147113434\bar{y} - 26.064581\bar{y}^2 + 12.7660158\bar{y}^3 \\ & - 0.184274863 \exp\left(\frac{0.5169435168 - \bar{y}}{0.04628266783}\right)^2. \end{aligned} \quad (10)$$

and SOC) of the electrodes, two distinct simulated short-circuit heat generation rates obtained by setting two different types of  $\phi_{s,p}(L,t)$  are expected. A comparison of the difference is shown in Section 3.3.

### 3.2. Electrochemical parameters validation

Various electrochemical parameters need to be determined in order to apply the porous electrode theory for modeling battery short-circuit. Although some of the parameters of LMO cells are provided by Ref. [22], there are still numerous electrochemical quantities that are specific to each cell, such as the SEI film resistance and the electrodes' volume fractions. These values could be obtained by comparing the simulated galvanostatic discharge curves with those obtained from our experiment.

In this experiment, the cell was discharged inside an oven of  $25.7^\circ\text{C}$  ambient temperature by connecting the battery to a charge/discharge station through electric wires that pass through the oven's door. The battery's output voltage and current during the test were carefully monitored and controlled by the equipment, respectively, to obtain reliable galvanostatic discharge curves of the cell.

On the other hand, the simulated discharge curves, recording the evolution of  $\phi_{s,p}(x,t)|_{x=L}$  against the cell capacity, can be plotted by solving the 14 time- and space-dependent variables (i.e.,

$\phi_{s,n}, \phi_{s,p}, \phi_{l,n}, \phi_{l,p}, \phi_{l,s}, C_{s,n}, C_{s,p}, C_n, C_p, C_s, j_n, j_p, U_n^c$ , and  $U_p^c$ ) in the porous electrode theory with the help of numerical iteration. The cell capacity is obtained from the product of the applied discharge current density  $I_s$  ( $\text{A m}^{-2}$ ), total effective interfacial area of cell  $A_{\text{cell}}$  ( $\text{m}^2$ ), and discharge time (in hours), where the 1C discharge current density,  $9.77 \text{ A m}^{-2}$ , is the value of  $I_s$  when the vertical drop of the simulated voltage occurs at precisely 3600 s. The value of  $A_{\text{cell}}$  could then be determined from dividing the cell's nominal capacity (5.25 Ah) by the 1C discharge current density and 1 h, gaining the value of  $A_{\text{cell}} = 0.537 \text{ m}^2$ . Our simulation result is shown Fig. 4, and the corresponding parameters and electrodes' open-circuit potentials (OCPs) are respectively presented in Table 1 and in Fig. 5.

### 3.3. Simulation result

By setting  $\phi_{s,p}(L,t) = 0.5 \exp(-0.07t)$  V as a boundary condition to the porous electrode model, the simulated short-circuit current density of the battery is shown in Fig. 6. A sudden drop of the current density in a few seconds after short-circuit takes place is observed. When the time is approximately 100 s, the sudden drop bends into a more gradual linear decline, then continuing in this way until zero is reached or calculation is terminated.

Fig. 7 shows a comparison of the simulated short-circuit heat generation rate ( $S_{sc}$ ) when  $\phi_{s,p}(L,t) = 0.5$  V and when  $\phi_{s,p}(L,t) = 0.5 \exp(-0.07t)$  V. Although the overall profiles of the two

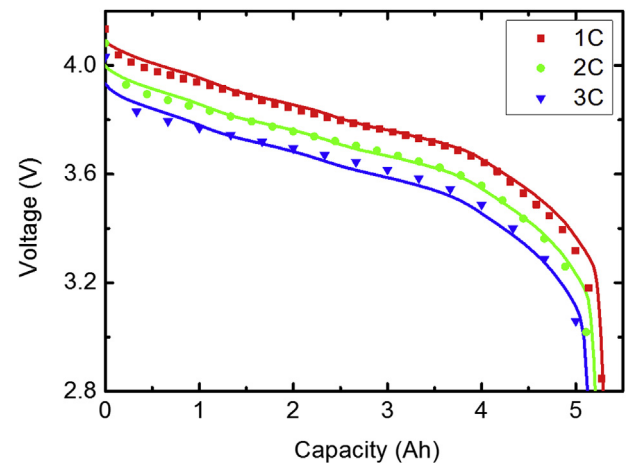


Fig. 4. The simulated (solid lines) and experimental (markers) discharge curves of the ITRI 5.25 Ah soft package prismatic cell. The effective interfacial area of cell,  $A_{\text{cell}}$ , is taken as  $0.537 \text{ m}^2$ .

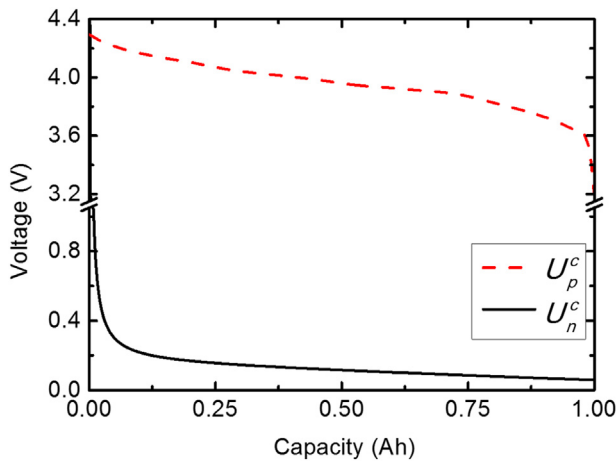
**Table 1**  
Electrochemical parameters for simulating the ITRI 5.25 Ah LMO cell.

Parameter	Negative electrode	Electrolyte electrode	Positive
$D_{s,i}$ ( $\text{m}^2 \text{s}^{-1}$ )	$2 \times 10^{-13a}$	—	$1 \times 10^{-13a}$
$R_{f,i}$ ( $\Omega \text{m}^2$ )	0.06 <sup>e</sup>	—	0
$\sigma_{s,i}$ ( $\text{S m}^{-1}$ )	100 <sup>a</sup>	—	3.8 <sup>a</sup>
$R_{s,i}$ ( $\mu\text{m}$ )	11 <sup>e</sup>	—	8.5 <sup>a</sup>
$\varepsilon_{s,i}$	0.410 <sup>e</sup>	—	0.297 <sup>e</sup>
$\varepsilon_{l,i}$	0.357 <sup>a</sup>	1	0.444 <sup>a</sup>
$c_{s,i}^M$ ( $\text{mol m}^{-3}$ )	17644 <sup>m</sup>	—	11636 <sup>m</sup>
$c_{s,i}^0$ ( $\text{mol m}^{-3}$ )	13223 <sup>m</sup>	—	228.16 <sup>m</sup>
$k_{s,i}$ ( $\text{m}^{2.5} \text{mol}^{-0.5} \text{s}^{-1}$ )	$2 \times 10^{-11e}$	—	$2 \times 10^{-11e}$
$L_i$ ( $\mu\text{m}$ )	74 <sup>m</sup>	20 <sup>m</sup>	107 <sup>m</sup>
$D_l$ ( $\text{m}^2 \text{s}^{-1}$ )	—	$3.227 \times 10^{-10e}$	—
$\kappa_l$ ( $\text{S m}^{-1}$ )	—	0.914 <sup>a</sup>	—
$t^+$	—	0.363	—
$T_{sc}^0$ ( $^\circ\text{C}$ )	—	25	—

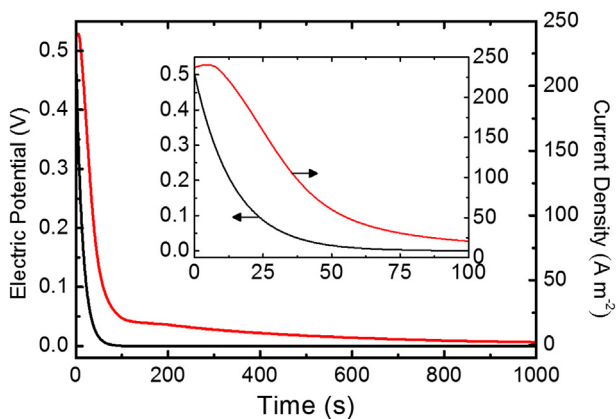
<sup>e</sup>Estimated.

<sup>m</sup>Measured.

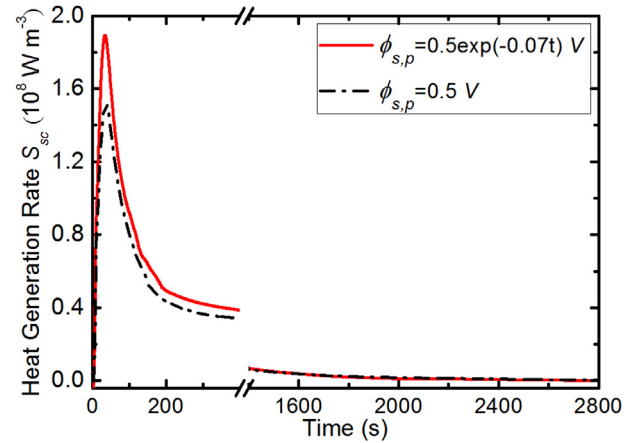
<sup>a</sup> Ref [22].



**Fig. 5.** The electrodes' OCPs of the ITRI LMO 5.25 Ah soft package prismatic cell.



**Fig. 6.** Assumed positive electrode's electric potential  $\phi_{s,p}(L,t) = 0.5\exp(-0.07t)$  V (black line) and the corresponding current density (red line) of the short-circuit cell when the temperature is kept constant (25.7  $^\circ\text{C}$ ) in the simulation. The inset is an enlarged plot of the two curves around the initial of the short circuit. (For interpretation of the references to color in this figure legend, the reader is referred to the web version of this article.)



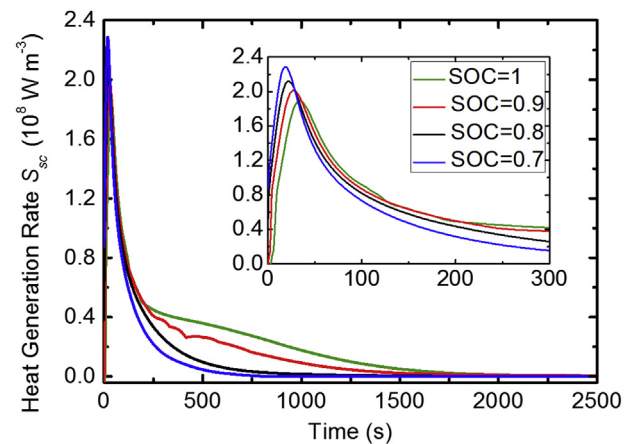
**Fig. 7.** Comparison of the simulated short-circuit heat generation rates ( $S_{sc}$ ) by applying the two different positive electrode's electric potential ( $\phi_{s,p}$ ) at 25.7  $^\circ\text{C}$ . The significant difference of the maximum values indicates that a precise description of  $\phi_{s,p}$  is critical.

illustration of short-circuit electric potential boundary condition is essential.

Other than the electric potential profile, the influences of SOC on battery heating can also be revealed by simulating short-circuit with the porous electrode theory. As demonstrated in Fig. 8, the maximum value of  $S_{sc}$  increases while SOC decreases, indicating that a more severe exothermic reaction occurs with smaller SOC. However, the reaction decays to zero more rapidly in comparison to a fully charged cell (SOC = 1), suggesting that the time interval of exothermic reaction reduces with SOC.

#### 4. Modeling battery thermal runaway

The oven test is frequently conducted to observe the safety of the cell under high temperature exposure. It reveals the overall thermal behavior of LIBs under thermal abuse condition. To give a complete illustration of the battery's thermal runaway behavior when it is exposed to elevated temperature, we adopted the thermal abuse equations [17,18] to simulate the thermal response of nail penetrated LIBs after thermal decomposing reactions in the cell is triggered.



**Fig. 8.** Short-circuit heat generation rates ( $S_{sc}$ ) of cells short-circuited at different SOC values when  $T = 25.7$   $^\circ\text{C}$ . Cells with smaller SOC values tend to have greater  $S_{sc}$  peak values, but they also decay more rapidly when compared with cells with greater SOC. The inset is an enlargement around the peaks of the curves.



#### 4.1. Model setup

The setup of the thermal-runaway model considers four reactions of the jelly-roll materials observed in previous studies: the SEI decomposition, the anode-electrolyte reaction, the cathode-electrolyte reaction, and the electrolyte decomposition reaction [17,18]. The characteristics of the reactions are dependent on their distinct material properties. Therefore, they are individually described by the four Arrhenius-type equation sets shown as follows:

##### I SEI decomposition

$$S_{\text{sei}} = H_{\text{sei}} W_{\text{c}} A_{\text{sei}} \exp \left[ \frac{-E_{\text{a,sei}}}{RT_{\text{ta}}} \right] c_{\text{sei}}^*, \quad (11)$$

$$\frac{dc_{\text{sei}}^*}{dt} = -A_{\text{sei}} \exp \left[ \frac{-E_{\text{a,sei}}}{RT_{\text{ta}}} \right] c_{\text{sei}}^*. \quad (12)$$

##### II Anode-electrolyte reaction

$$S_{\text{n}} = H_{\text{n}} W_{\text{c}} A_{\text{n}} \exp \left[ \frac{-z}{z^0} \right] \exp \left[ \frac{-E_{\text{a,n}}}{RT_{\text{ta}}} \right] c_{\text{n}}^*, \quad (13)$$

$$\frac{dc_{\text{n}}^*}{dt} = -A_{\text{n}} \exp \left[ \frac{-z}{z^0} \right] \exp \left[ \frac{-E_{\text{a,n}}}{RT_{\text{ta}}} \right] c_{\text{n}}^*, \quad (14)$$

$$\frac{dz}{dt} = A_{\text{n}} \exp \left[ \frac{-z}{z^0} \right] \exp \left[ \frac{-E_{\text{a,n}}}{RT_{\text{ta}}} \right] c_{\text{n}}^*. \quad (15)$$

##### III Cathode-electrolyte reaction

$$S_{\text{p}} = H_{\text{p}} W_{\text{p}} A_{\text{p}} \alpha (1 - \alpha) \exp \left[ \frac{-E_{\text{a,p}}}{RT_{\text{ta}}} \right], \quad (16)$$

$$\frac{d\alpha}{dt} = R_{\text{p}} = A_{\text{p}} \alpha (1 - \alpha) \exp \left[ \frac{-E_{\text{a,p}}}{RT_{\text{ta}}} \right]. \quad (17)$$

##### IV Electrolyte decomposition

$$S_{\text{e}} = H_{\text{e}} W_{\text{e}} A_{\text{e}} \exp \left[ \frac{-E_{\text{a,e}}}{RT_{\text{ta}}} \right] c_{\text{e}}^*, \quad (18)$$

$$\frac{dc_{\text{e}}^*}{dt} = -A_{\text{e}} \exp \left[ \frac{-E_{\text{a,e}}}{RT_{\text{ta}}} \right] c_{\text{e}}^*. \quad (19)$$

The readers are referred to [17,18] for a detailed description of the physical interpretations of the four sets of reaction kinetics.

#### 4.2. Characteristics of heat generation

With the help of the parameters and initial values shown in Tables 2 and 3, respectively, the four heat generation rate profiles of the thermal abuse equation set, i.e.  $S_{\text{sei}}$ ,  $S_{\text{n}}$ ,  $S_{\text{p}}$ , and  $S_{\text{e}}$ , can be obtained. In order to clarify the different temperatures that initiate the exothermic reactions, we give a temperature sweep of  $1^\circ\text{C s}^{-1}$  to observe the onset of the action. Simulation results of the ITRI 5.25 Ah LMO cell are shown in Fig. 9, and the heat generation characteristics of the four reactions, including triggering temperature and the whole profile, can be clearly demonstrated. In addition, since the positive electrode's material is LMO, a greater peak of  $S_{\text{p}}$ , compared to [17,18], is obtained based on the material parameters provided by Ref. [43].

From the result of assigning temperature sweep, we select a specific heat generation rate of  $10^5 \text{ W m}^{-3}$ , above which the individual reactions are triggered. Due to its unstable nature, the SEI decomposition occurs at the lowest temperature value of the four reactions at  $128^\circ\text{C}$ , as shown in Fig. 9. Closely following behind is the anode-electrolyte reaction with the triggering temperature of  $146^\circ\text{C}$ . The cathode-electrolyte reaction takes place at around  $182^\circ\text{C}$ , showing the most severe exothermic reaction, and the electrolyte decomposition occurs last at approximately  $229^\circ\text{C}$ . It must be noted that different LIBs ought to have different heat generation characteristics. Batteries with various shapes and sizes, or even with novel safety designs, are also critical to the determination of battery thermal runaway. By altering the frequency factor  $E_{\text{a,i}}$  or the activation energy  $A_{\text{i}}$ , one can modulate the triggering temperature and the overall exothermic reaction profile of individual batteries to fit the results obtained from Differential Scanning Calorimetry (DSC) or other tests.

### 5. Modeling nail penetration

Generally, the nail penetration process of LIBs, which involves a dramatic change in temperature, is the coalescence of two major mechanisms: short-circuit of LIB, where it happens near the nail-battery interface, and the decomposition of jelly-roll materials, occurring within the whole cell. They were respectively described in Sections 3 and 4. However, to provide a more thorough modeling framework of the nail penetration test, we construct a compact model that simulates the nail penetration test of LIBs by coupling the two major mechanisms.

#### 5.1. Model setup

In order to simulate the battery temperature distribution, a three-dimensional geometry of the ITRI 5.25 Ah soft package prismatic cell nail penetration test is constructed, and the schematic diagram is shown in Fig. 10. Several simplifications and assumptions of the original complex geometry are made as they are peripheral factors or do not have significant effect to the modeling, as stated in the following. The current collector tabs and the spirally

**Table 2**  
Parameters for the thermal abuse model equations obtained from Refs. [17,18].

Parameter	SEI decomposition	Anode-electrolyte reaction	Cathode-electrolyte reaction	Electrolyte decomposition
$H_i (\text{J g}^{-1})$	257	1714	400 <sup>a</sup>	155
$W_i (\text{kg m}^{-3})$	$6.104 \times 10^2$	$6.104 \times 10^2$	$1.438 \times 10^{3\text{e}}$	$4.069 \times 10^2$
$A_i (\text{s}^{-1})$	$1.667 \times 10^{15}$	$2.5 \times 10^{13}$	$6.667 \times 10^{13}$	$5.14 \times 10^{25}$
$E_i (\text{J mol}^{-1})$	$1.3508 \times 10^5$	$1.3508 \times 10^5$	$1.396 \times 10^5$	$2.74 \times 10^5$

<sup>e</sup>Estimated.

<sup>a</sup> Ref [43].

**Table 3**  
Initial values for thermal abuse model variables [17,18].

Variable	Initial value
$c_{\text{sei}}^*$	0.15
$c_{\text{n}}^*$	0.75
$c_{\text{e}}^*$	1
$z$	0.033
$\alpha$	0.04
$T_{\text{ta}} (^\circ\text{C})$	25.7

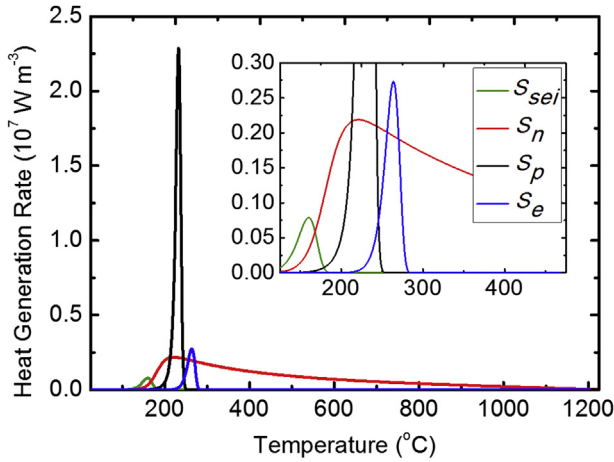


**Fig. 9.** The heat generation rate profiles of the thermal abuse model, i.e.  $S_{sei}$ ,  $S_n$ ,  $S_p$ , and  $S_e$ , by applying a temperature sweep of  $1\text{ }^{\circ}\text{C s}^{-1}$ . The cathode-electrolyte reaction ( $S_p$ ) manifests the most severe exothermic reaction of the four. The inset is an enlargement around the peaks of the four rates.

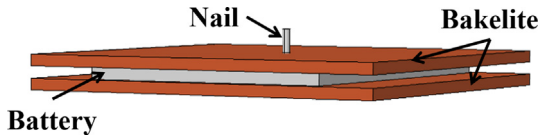


**Fig. 10.** Schematic diagram of the three dimensional nail penetration model setup.

wound geometry of the jelly-roll inside the cell are neglected. The prismatic cell is treated as a bulk and the thermal properties are volume-averaged values. Since the packaging material is thin, the aluminum foil wrapping is disregarded. No dilation of the prismatic cell is assumed due to the two fixed Bakelite in the actual test and the difficulty of constructing a deformable geometry. The influence of the steel bolts for fastening the two Bakelite is not considered. All the materials used in the three-dimensional geometry are regarded as homogeneous and isotropic, with their thermal properties shown in Table 4.

The nail diameter is a geometry feature that cannot be neglected, since it determines the total area of short-circuit in the nail penetration test. As can be expected, a larger short-circuit area causes a greater risk of inflammation or explosion. Moreover, studies have pointed out that the nail can also dissipate considerable amount of heat, which may retard the temperature rising rate of the cell and reduce the risk of thermal runaway [39,40]. When a cylindrical nail is penetrated into the LIB, short-circuit is assumed to occur only at the interface between the penetrated nail and the battery. Hence, it is plausible to propose the short-circuit heat generation rate per unit area,  $S_{sc}^{surf}$ , as

$$S_{sc}^{surf} = \frac{1}{2} r_{nail} S_{sc}, \quad (20)$$

**Table 4**  
Thermal properties of objects used in the nail penetration test.

Parameter	Nail	Bakelite	Jelly-roll
$k_i$ ( $\text{W m}^{-1} \text{K}^{-1}$ )	44.5	0.385	0.034 <sup>a</sup>
$\rho_i$ ( $\text{kg m}^{-3}$ )	7850	1318	1700 <sup>a</sup>
$C_{p,i}$ ( $\text{J kg}^{-1} \text{K}^{-1}$ )	475	14.4	830 <sup>a</sup>

<sup>a</sup> Ref [17].

which transforms the heat generation per unit volume to that per unit area of the interface. This  $S_{sc}^{surf}$  will serve as the boundary heat source at the nail and battery junction in our modeling.

With the heat generation rate from battery short-circuit and thermal abuse equations, the temperature distribution of the constructed three-dimensional geometry is calculated by thermal energy balance between the generated and dissipated heat in the  $i$ -th mesh element [41,42]:

$$\rho_i C_{p,i} \frac{\partial T_i}{\partial t} = -\nabla \cdot (k_i \nabla T_i) + \sum_j S_j, \quad (21)$$

where  $j = sei, n, p$ , and  $e$ , and  $\nabla$  is the gradient operator for the three-dimensional geometry's Cartesian coordinate. Furthermore, convective cooling is applied to all the geometry's surfaces that are exposed to the ambient:

$$q^{conv} = h(T^{surf} - T^{amb}), \quad (22)$$

where  $h$  is the heat transfer coefficient and the ambient temperature  $T^{amb}$  is assumed to remain constant at the initial value ( $25.7\text{ }^{\circ}\text{C}$ ) throughout the test.

Through Equation (21), the equations for simulating battery short-circuit and thermal runaway could therefore be coupled together. Their connection is shown in Fig. 11, where short-circuit and thermal abuse equations calculate their corresponding heat generation rates, and the time-space variation of cell temperature is evaluated via thermal energy balance. The calculated temperature is treated as a variable that is substituted back into the corresponding equations, where they calculate and return the updated heat generation rates to Equations (21) and (22), allowing the cell temperature distribution of the next time step to be evaluated.

Although the simulation of battery short-circuit and thermal abuse require the input of temperature, it should be noted that the heat generated by battery short-circuit is applied only at the nail-battery interface, whereas thermal abuse is in accordance with the battery's bulk geometry. Accordingly, the temperature values for the two equation sets should have distinct locations as their source. The temperature for battery short-circuit,  $T_{sc}$ , is taken as the domain-averaged value at the nail-battery interface. As will be shown later,  $T_{sc}$  has a maximum value of over  $400\text{ }^{\circ}\text{C}$  during the nail penetration process. On the other hand, it has been shown that once the temperature at arbitrary location in the jelly-roll exceeds the material decomposition triggering value, a whole cell thermal runaway is likely to occur [9]. As a result, the temperature for thermal abuse model,  $T_{ta}$ , is taken as the maximum value of the whole cell to probe for any temperature that can activate the thermal abuse reactions.

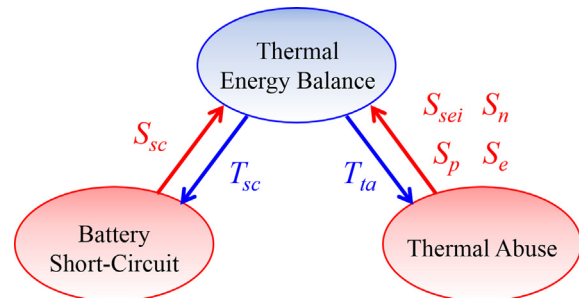


**Fig. 11.** Coupling between the short-circuit and the thermal abuse modelings via thermal energy balance equation in the nail penetration simulation.

## 5.2. Simulation result

By coupling battery short-circuit and thermal abuse through the thermal energy balance equation, the simulation result of the ITRI 5.25 Ah soft package prismatic cell nail penetration test is presented in Fig. 12. As shown in the diagram, a large current density from the battery is observed due to short-circuit occurrence in the test. However, the current drops to almost 20% of its initial value after 400 s, because of the depleting active material initially intercalated in the anode. Coexisting with the large output current is the severe short-circuit exothermic reaction at the nail-battery interface, which includes the Joule heating and the entropic heating of lithium redox reaction as shown in Equation (8). The short-circuit exothermic heat generation rate  $S_{sc}$  reaches its maximum value at around 125 s and decays gradually with time, estimated to also result from depletion of the active material. An abrupt drop of current density and jump of heat generation rate at 50 s are also observed in the figure. The cause of this unexpected variation is explained later in this section with further observation of other variables in the model.

During the initial stage with only the occurrence of nail penetration and no thermal runaway, short-circuit heat generation rate provides the initial heating of the cell at the nail-battery interface. Accordingly, the two distinct temperatures for the two models,  $T_{sc}$  and  $T_{ta}$ , rise, as presented in Fig. 13. The two temperatures have an overall similar behavior within the interval of calculation. However,  $T_{ta}$  instantly jumps to approximately 450 °C at 50 s while  $T_{sc}$  continues in a more gradual path to its maximum value of just above 400 °C. The departure of the two temperatures ends at about 75 s, and continues in a nearly identical path until the end of calculation. The instant jump of the temperature at 50 s could be explained by observing Fig. 14, which illustrates the thermal runaway heat generation rate profiles with specifying  $T_{ta}$  as its temperature. By comparing this result with the one that was not coupled (Fig. 9), the thermal runaway heat generation rate profiles based on the  $T_{ta}$  value (Fig. 14) are more concentrated than those of temperature sweep in the oven test, indicating that main part of the exothermic reaction happens within a short time interval, specifically at around 50 s. This characteristic reveals the reason for the unexpected variations at 50 s of short-circuit current density and heat generation rate in Fig. 12. It can also explain the departure of  $T_{sc}$  and  $T_{ta}$  at the same second, since it is the moment when whole cell thermal runaway occurs.

Simulated spatio-temporal variation of cell temperature during the nail penetration process is demonstrated in Fig. 15. At 45 s, the

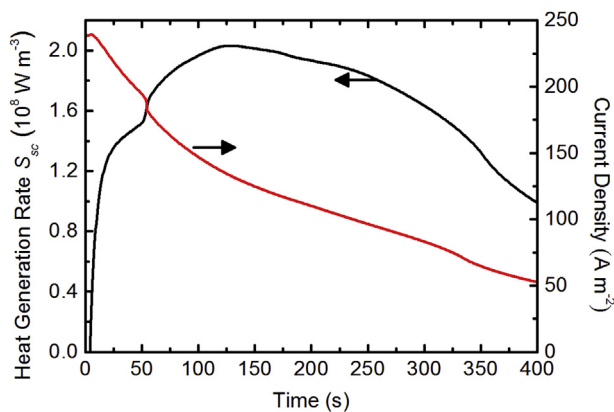


**Fig. 12.** Simulated short-circuit heat generation rate ( $S_{sc}$ ) and current density of the nail penetration test by coupling the battery short-circuit and thermal abuse equations. The nail penetration occurs at 0 s.

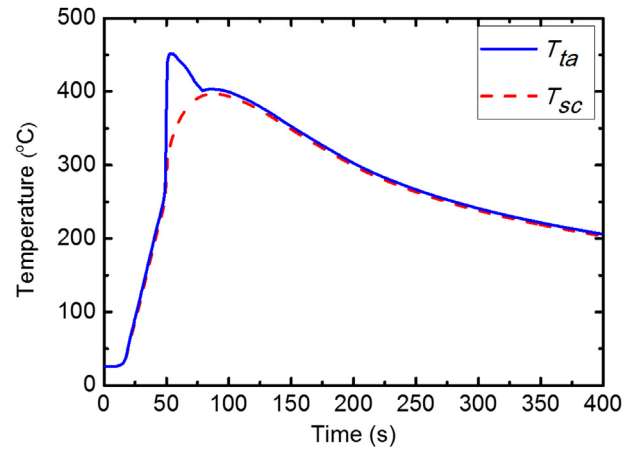


**Fig. 13.** Comparison of  $T_{sc}$  and  $T_{ta}$ . The two curves present a similar profile until about 50 s, indicating the occurrence of an additional exothermic reaction other than short circuit.

heating of the cell is contributed by short-circuit heat generation rate, forming a local hot spot at the point of penetration. Thermal runaway occurs at 50 s, causing the temperature of the whole cell to rise abruptly. Due to the heat conduction lag, maximum surface temperature of the cell is detected at 60 s. After 60 s, convection mechanism determines the temperature variation of the cell since the thermal abuse heat generation rate dies out quickly after its short occurrence.

Referring to the experimental results, we capture the simulated temperature time variation data at spots corresponding to the experiment thermal couple locations. The compared simulation and experiment results are shown in Fig. 16. Since thermal couples A and B (as well as C and D) are located at symmetric positions, we only present the data obtained from one of the spots to represent our simulation result. To verify the obtained temperature profiles from simulation, there are three indexes that can be compared with the experimental data. First, the slopes of the temperatures at thermal runaway obtained from the experiments are nearly vertical. The simulation traces out this characteristic successfully since most of the heat generation reaction concentrates in a narrow time interval (Fig. 14). Second, temperature from thermal

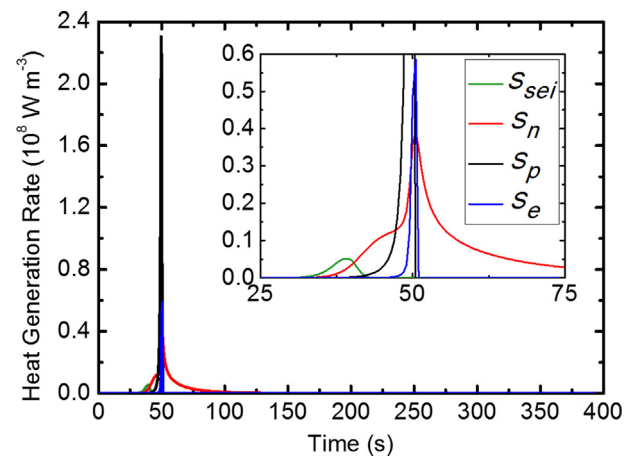


**Fig. 14.** Simulated heat generation rate profiles of the thermal abuse model by integrating short-circuit electrochemical model and the thermal abuse model. Almost all the exothermic reactions are concentrated in a short time interval, pointing out the occurrence of a severe whole cell thermal runaway at the instant. The inset is the enlarged plot around the moment of thermal runaway.



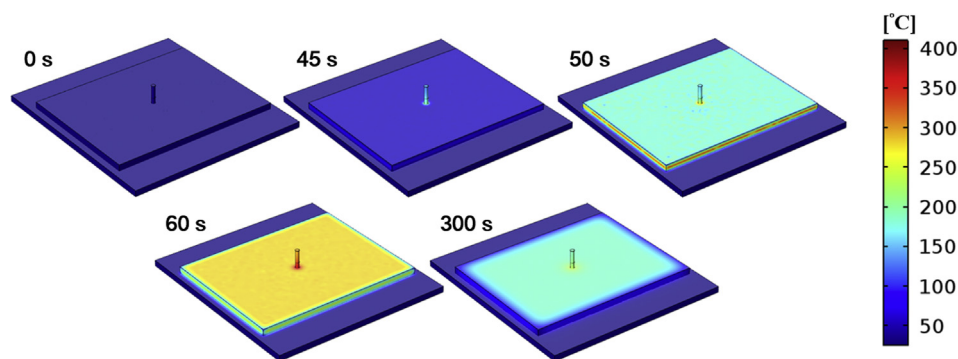


Fig. 15. Simulated spatio-temporal temperature in the nail penetration test.

couple E, which is nearest to the penetration point, peaks at 310.6 °C. The simulation reveals a maximum temperature of 327.3 °C, a 5.38% error, from the temperature profile corresponding to thermal couple E. Third, the profiles of temperature drop after the apex are primarily determined by the ambient conditions. Since ventilation of the chamber is turned on after the penetration, a convection cooling will occur. A cooling boundary condition, which is then set with the heat transfer coefficient at a higher value of  $h = 71.7 \text{ W m}^{-2} \text{ K}^{-1}$  (compared with  $h \approx 7.6 \text{ W m}^{-2} \text{ K}^{-1}$  for natural convection), produces a temperature profile that fits well with the experimental results.

## 6. Conclusion

We have proposed a novel method by using the porous electrode theory to model the electrochemical processes of short-circuited LIBs. By doing so, we have calculated the output current of short-circuit batteries and predicted the heat generation rates of cells with different electrochemical parameters, such as SOC. In addition, with the battery thermal abuse equations from the oven test, we have also simulated the thermal runaway behavior of LIBs.

By combining the two modelings, our simulation result of cell temperature variation shows great similarity with the nail penetration test. Therefore, we believe this method is capable to accurately model LIB nail penetration tests. Furthermore, our model can be extended to predict the effectiveness of LIBs with certain safety features, such as cells with additives that can shut down the mass or charge transfer process when the battery is short-circuited. Finally, regarding cases where a nail is penetrated into cells with new electrodes/electrolytes or cells that are cycled, preliminary experiments are required to obtain the parameters of cells with new materials, and additional models need to be constructed to describe jelly-roll deterioration after cycling tests. Future work will explore these issues in more detail.

## Acknowledgments

This work was supported by the R.O.C. National Science Council under Grant NSC-101-2221-E-002-139.

## References

- [1] J. Tollefson, *Nature* 456 (2008) 436–440.
- [2] K. Kang, Y.S. Meng, J. Bréger, C.P. Grey, G. Ceder, *Science* 311 (2006) 977–980.
- [3] S.I. Tobishima, K. Takei, Y. Sakurai, J.I. Yamaki, *J. Power Sources* 90 (2000) 188–195.
- [4] K. Kitoh, H. Nemoto, *J. Power Sources* 81–82 (1999) 887–890.
- [5] Y.K. Sun, S.T. Myung, B.C. Park, J. Prakash, I. Belharouak, K. Amine, *Nat. Mater* 8 (2009) 320–324.
- [6] K. Amine, I. Belharouak, Z.H. Chen, T. Tran, H. Yumoto, N. Ota, S.T. Myung, Y.K. Sun, *Adv. Mater.* 22 (2010) 3052–3057.
- [7] S. Al Hallaj, H. Maleki, J.S. Hong, J.R. Selman, *J. Power Sources* 83 (1999) 1–8.
- [8] Q. Wang, P. Ping, X. Zhao, G. Chu, J. Sun, C. Chen, *J. Power Sources* 208 (2012) 210–224.
- [9] T. Yamauchi, K. Mizushima, Y. Satoh, S. Yamad, *J. Power Sources* 136 (2004) 99–107.
- [10] S. Santhanagopalan, P. Ramadass, J. Zhang, *J. Power Sources* 194 (2009) 550–557.
- [11] R.M. Spotnitz, J. Weaver, G. Yeduvaka, D.H. Doughty, E.P. Roth, *J. Power Sources* 163 (2007) 1080–1086.
- [12] D.H. Doughty, P.C. Butler, R.G. Jungst, E.P. Roth, *J. Power Sources* 110 (2002) 357–363.
- [13] G. Nagasubramanian, D. Ingersoll, D. Doughty, D. Radzykewycz, C. Hill, C. Marsh, *J. Power Sources* 80 (1999) 116–118.
- [14] E.P. Roth, D.H. Doughty, *J. Power Sources* 128 (2004) 308–318.
- [15] W. Cai, H. Wang, H. Maleki, J. Howard, E. Lara-Curzio, *J. Power Sources* 196 (2011) 7779–7783.
- [16] C.J. Mikolajczak, T. Hayes, M.V. Megerle, M. Wu, in: *PORTABLE07. IEEE International Conference on Portable Information Devices*, 2007, pp. 1–6.
- [17] T. Hatchard, D. MacNeil, A. Basu, J. Dahn, *J. Electrochem. Soc.* 148 (2001) A755–A761.
- [18] G.H. Kim, A. Pesaran, R. Spotnitz, *J. Power Sources* 170 (2007) 476–489.
- [19] J. Newman, W. Tiedemann, *AIChE J.* 21 (1975) 25–41.
- [20] J. Newman, K. Thomas-Alyea, *Electrochemical Systems*, third ed., Wiley-Interscience, Hoboken, NJ, 2004.
- [21] T.F. Fuller, M. Doyle, J. Newman, *J. Electrochem. Soc.* 141 (1994) 1–10.
- [22] M. Doyle, J. Newman, A.S. Gozdz, C.N. Schmutz, J.M. Tarascon, *J. Electrochem. Soc.* 143 (1996) 1890–1903.

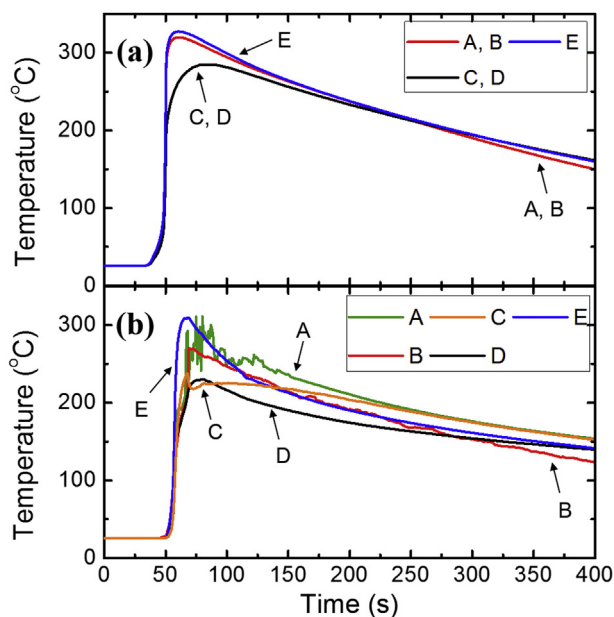


Fig. 16. Comparison of the (a) simulated and (b) experimental results. The results show good agreement on describing the temperature rise, the maximum temperature, and the temperature declination due to ventilation.

- [23] P. Arora, M. Doyle, A.S. Gozdz, R.E. White, J. Newman, J. Power Sources 88 (2000) 219–231.
- [24] T.S. Dao, C.P. Vyasarayani, J. McPhee, J. Power Sources 198 (2004) 329–337.
- [25] M. Guo, G. Sikha, R.E. White, J. Electrochem. Soc. 158 (2011) A122–A132.
- [26] L. Cai, R.E. White, J. Power Sources 196 (2011) 5985–5989.
- [27] S. Santhanagopalan, R.E. White, Int. J. Energy Res. 34 (2010) 152–163.
- [28] E. Sahraei, J. Campbell, T. Wierzbicki, J. Power Sources 220 (2012) 360–372.
- [29] M.S. Wu, P.C. Chiang, J.C. Lin, Y.S. Jan, Electrochim. Acta 49 (2004) 1803–1812.
- [30] D. Bernardi, E. Pawlikowski, J. Newman, J. Electrochem. Soc. 132 (1985) 5–12.
- [31] X.W. Zhang, Electrochim. Acta 56 (2011) 1246–1255.
- [32] D.H. Jeon, S.M. Baek, Energy Convers. Manag. 52 (2011) 2973–2981.
- [33] K. Smith, G.H. Kim, E. Darcy, A. Pesaran, Int. J. Energy Res. 34 (2010) 204–215.
- [34] L. Cai, R.E. White, J. Electrochem. Soc. 157 (2010) A1188–A1195.
- [35] W.F. Fang, O.J. Kwon, C.Y. Wang, Int. J. Energy Res. 34 (2010) 107–115.
- [36] S.A. Khateeb, M.M. Farid, J.R. Selman, S. Al Hallaj, J. Power Sources 158 (2006) 673–678.
- [37] M.S. Wu, K.H. Liu, Y.Y. Wang, C.C. Wan, J. Power Sources 109 (2002) 160–166.
- [38] V. Srinivasan, C.Y. Wang, J. Electrochem. Soc. 150 (2003) A98–A106.
- [39] H. Maleki, J.N. Howard, J. Power Sources 191 (2009) 568–574.
- [40] T.G. Zavalis, M. Behm, G. Lindbergh, J. Electrochem. Soc. 159 (2012) A848–A859.
- [41] G. Luo, C.Y. Wang, in: X. Yuan, H. Liu, J. Zhang (Eds.), Lithium-ion Batteries: Advanced Materials and Technologies, CRC Press, Boca Raton, FL, 2011, pp. 303–326.
- [42] Y.F. Chen, J.W. Evans, J. Electrochem. Soc. 141 (1994) 2947–2955.
- [43] R. Spotnitz, J. Franklin, J. Power Sources 113 (2003) 81–100.
- k*: heat transfer coefficient,  $\text{W m}^{-1} \text{K}^{-1}$
- k<sub>s</sub>*: reaction rate constant,  $\text{m}^{2.5} \text{mol}^{-0.5} \text{s}^{-1}$
- L*: thickness, m
- r<sub>nail</sub>*: nail radius, m
- R*: gas constant,  $8.314 \text{ J K}^{-1} \text{mol}^{-1}$
- R<sub>f</sub>*: SEI film resistance,  $\Omega \text{m}^2$
- R<sub>s</sub>*: radius of electrode particle,  $\mu\text{m}$
- S*: heat generation rate,  $\text{W m}^{-3}$
- T*: temperature, K
- t*: time, s
- t<sup>+</sup>*: transference number
- U<sup>c</sup>*: open-circuit potential at 25 °C, V
- W*: active content density,  $\text{kg m}^{-3}$
- $\bar{x}$ : state of charge of negative electrode
- $\bar{y}$ : state of charge of positive electrode
- z*: dimensionless SEI thickness
- $\alpha$ : degree of conversion
- v<sub>f</sub>*: Filler volume fraction
- v<sub>l</sub>*: electrolyte volume fraction
- v<sub>s</sub>*: porous electrode volume fraction
- $\phi_l$ : electric potential of electrolyte phase, V
- $\phi_s$ : electric potential of solid phase, V
- $\gamma$ : Bruggeman exponential coefficient, 1.5
- $\eta_s$ : surface over-potential, V
- $\kappa_l$ : electrolyte phase ionic conductivity,  $\text{S m}^{-1}$
- $\rho$ : density,  $\text{kg m}^{-3}$
- $\sigma_s$ : solid phase electric conductivity,  $\text{S m}^{-1}$

## Nomenclature

*a*: specific interfacial area,  $\text{m}^2 \text{m}^{-3}$

*A*: frequency factor,  $\text{s}^{-1}$

*A<sub>cell</sub>*: total effective interfacial area of cell,  $\text{m}^2$

*c*: concentration of salt in electrolyte,  $\text{mol m}^{-3}$

*c<sub>s</sub>*: concentration of lithium in electrode,  $\text{mol m}^{-3}$

*c<sub>e</sub>*: dimensionless concentration of electrolyte

*c<sub>n</sub><sup>\*</sup>*: dimensionless amount of Li intercalated within the carbon

*c<sub>sei</sub><sup>\*</sup>*: dimensionless amount of SEI Li-containing metastable species

*C<sub>p</sub>*: heat capacity,  $\text{J kg}^{-1} \text{K}^{-1}$

*D<sub>l</sub>*: electrolyte phase lithium-ion diffusivity,  $\text{m}^2 \text{s}^{-1}$

*D<sub>s</sub>*: solid phase lithium diffusivity,  $\text{m}^2 \text{s}^{-1}$

*E<sub>0</sub>*: activation energy,  $\text{J mol}^{-1}$

*F*: Faraday constant,  $96485 \text{ C mol}^{-1}$

*H*: specific energy,  $\text{J g}^{-1}$

*h*: heat transfer coefficient,  $\text{W m}^{-2} \text{K}^{-1}$

*I<sub>l</sub>*: electrolyte phase current density,  $\text{A m}^{-2}$

*I<sub>s</sub>*: solid phase current density,  $\text{A m}^{-2}$

*j<sub>Li</sub>*: pore wall flux of lithium-ion,  $\text{mol m}^{-2} \text{s}^{-1}$

## Subscript

*e*: separator region

*i*: for component, species, or reaction *i*

*n*: negative electrode

*p*: positive electrode

*sc*: short-circuit

*ta*: thermal abuse

*cell*: battery

*sei*: solid-electrolyte interface

## Superscript

*0*: initial state

*M*: maximum

*eff*: effective

*amb*: ambient

*surf*: surface